ISSN 0020-4412, Instruments and Experimental Techniques, 2014, Vol. 57, No. 2, pp. 103–119. © Pleiades Publishing, Ltd., 2014.
Original Russian Text © O.V. Andreeva, M.B. Golubeva, F.F. Guber, A.P. Ivashkin, A. Krasa, A. Kugler, A.B. Kurepin, O.A. Petukhov, A.I. Reshetin, A.S. Sadovsky, O. Svoboda, Yu.G. Sobolev, P. Tlusty, E.A. Usenko, 2014, published in Pribory i Tekhnika Eksperimenta, 2014, No. 2, pp. 13–30.

NUCLEAR
EXPERIMENTAL TECHNIQUES

Forward Scintillation Hodoscope for Nuclear Fragment Detection at the High Acceptance Dielectron Spectrometer (HADES) Setup

O. V. Andreeva[a], M. B. Golubeva[a], F. F. Guber[a], A. P. Ivashkin[a], A. Krasa[b], A. Kugler[b], A. B. Kurepin[a], O. A. Petukhov[a], A. I. Reshetin[a], A. S. Sadovsky[a], O. Svoboda[b], Yu. G. Sobolev[b], P. Tlusty[b], and E. A. Usenko[a]

[a] *Institute for Nuclear Research, Russian Academy of Sciences, pr. Shestidesyatiletiya Oktyabrya 7a, Moscow, 117312 Russia*

[b] *Nuclear Physics Institute ASCR, Rez, CZ25068 Czech Republic*

Received June 28, 2013

Abstract—The main characteristics of the forward scintillation hodoscope and readout electronics of the high acceptance dielectron spectrometer (HADES) at GSI (Darmstadt, Germany) are presented. Methods for adjustment and amplitude–time calibration of hodoscope detectors using cosmic rays and results of measurements of the Au + Au reaction at a beam energy of 1.24 GeV/nucleon are described. The use of the forward hodoscope for tagging the $n + p$ reaction by means of the deuteron beam incident on a liquid hydrogen target is discussed. A procedure for determining the reaction plane angle in event-by-event analysis of the Au + Au reaction data (at 1.24 GeV/nucleon) is presented.

DOI: 10.1134/S0020441214020146

1. INTRODUCTION

Studying the nuclear matter properties in wide ranges of temperatures and densities is a very important direction of modern relativistic nuclear physics. The underlying reason for carrying out experiments in this field of physics is the possibility of studying the nuclear matter state equation and verifying the predictions of the basic theory of strong interactions—quantum chromodynamics. Studying the state equation of strongly interacting matter is also important for understanding the physical processes in neutron stars and supernovae [1].

The active development of the experimental program over the past 20 years was largely determined by the progress in designing high-power accelerators and the feasibility of measurements at higher energies. Beginning with the pioneer experiment of the Dilepton Spectrometer (DLS) at the Bevalac accelerator (Berkeley, United States), in which nuclear collisions were investigated at a energy of 1 GeV/nucleon [2], a number of experiments (CERES, NA49, NA50/60, etc.) were carried out at the energy $\sqrt{s} = 17$ GeV at the Super Proton Synchrotron (SPS) accelerator (CERN, Switzerland). Experiments at energies as high as $\sqrt{s} =$ 200 GeV (PHENIX and STAR) are currently under way at the Relativistic Heavy Ion Collider (RHIC) (Brookhaven, United States). The first experiments on the collisions of lead nuclei at energies $\sqrt{s} = 2.76$ TeV were performed at the CMS, ATLAS, and ALICE setups of the LHC collider (CERN). It is expected that experimental data on nuclear collisions with energies as high as 7 TeV in the center-of-mass system will be obtained at these setups in the near future.

All high-energy experiments are aimed at searching for signals indicating the production of a new state of nuclear matter under the conditions of high temperature and density, i.e., the production of the so-called quark–gluon plasma. At the same time, the nuclear matter properties can be modified as early as at moderate densities and temperatures in nucleus–nucleus collisions at energies of ≥1 GeV/nucleon. This modification may manifest itself in partial restoration of the chiral symmetry.

The experiment at the high acceptance dielectron spectrometer (HADES) at GSI (Darmstadt, Germany) occupies a highly important place among these experiments. Both charged hadrons (protons, pions, and kaons) and electron–positron pairs from decays of light vector mesons produced by nuclear collisions at energies of up to 2 GeV/nucleon are measured in this experiment. Since electrons and positrons do not suffer nuclear interaction, they carry the most direct and ungarbled information on the modification of the hadron properties in nuclear matter, such as the hadron mass and decay width. The other feature of this experiment is the possibility of studying the nuclear properties not only in nucleus–nucleus reactions, but also in hadron–nucleus and elementary hadron–hadron collisions on the proton beams with energies as high as 4 GeV and pions with energies as high as 2 GeV. It is thereby possible to obtain and compare information on the hadron properties in cold, hot, and dense nuclear matter with the minimum systematic errors.

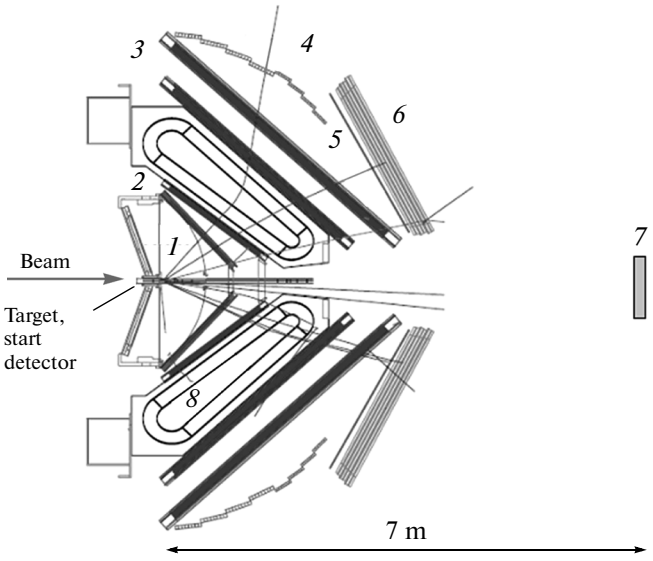

Fig. 1. Layout of the HADES setup: (*1*) ring-imaging Cherenkov detector (RICH), (*2*, *3*) mini-drift chambers (MDCI/II and MDCIII/IV, respectively), (*4*) time-of-flight scintillation hodoscope (TOF), (*5*) forward time-of-flight scintillation hodoscope (TOFINO), (*6*) pre-shower detector, (*7*) forward hodoscope (FW), and (*8*) superconducting magnet.

In this paper, we describe the forward multichannel scintillation hodoscope, which is one of the most important detector subsystems of the HADES. For the first time, this hodoscope was used to tag the reaction of electron–positron pair production in interactions of the incident quasi-free 1.25-GeV neutrons with protons of the liquid-hydrogen target. Tagging of the interaction between quasi-free neutrons and protons is based on reaction $dp \longrightarrow np + p_{spect}$, where p_{spect} is the spectator proton, i.e., a proton from an incident deuteron nucleus that does not participate in the interaction with the target's proton and is detected by the forward hodoscope.

Being substantially upgraded in recent years, the forward hodoscope was used in the experiment on studying electron–positron pair production in the Au + Au reaction at 1.24-GeV/nucleon energies of incident Au nuclei. This experiment was conducted in the middle of 2012, and the data obtained in it have been analyzed today. The main function of the forward hodoscope in this experiment was to determine the reaction plane in event-by-event data analysis in order to obtain information on charged particle fluxes in this reaction.

A brief description and the main characteristics of the HADES are presented below, in Section 2. The forward scintillation hodoscope and its performance characteristics are described in Section 3. Readout electronics for hodoscope detector signals and its integration into the HADES data acquisition system are discussed in Section 4. Section 5 presents procedures for adjustment of the hodoscope detectors and their time and amplitude calibration using cosmic rays and experimental data obtained in the Au + Au reaction at a beam energy of 1.24 GeV/nucleon. The application of the forward hodoscope for tagging the *np* reaction using the deuteron beam incident on a liquid-hydrogen target is discussed in Section 6. A method for determining the reaction plane angle in event-by-event analysis of Au + Au reaction data (at 1.24 GeV/nucleon) is stated, and factors effecting the accuracy in reconstructing this angle are discussed in Section 7.

2. HADES SETUP

The HADES setup [3] is a wide-aperture magnetic spectrometer for identifying and measuring the charged hadron momenta and the invariant mass of electron–positron pairs produced in nucleus–nucleus interactions at incident nuclei energy of 1–2 GeV/nucleon and in hadron–nucleus interactions at incident hadron energy as high as 4 GeV.

Physically, the spectrometer is azimuthally divided into six identical sectors that are determined by the location of the superconducting toroidal magnet windings and cover the region of polar angles of 18°–88° and almost the complete azimuthal angle. The cross section of two opposite sectors is shown in Fig. 1. Under these conditions, the spectrometer has a high (~40%) geometrical efficiency in the intermediate rapidity range for dilepton pairs.

There are several subsystems in the spectrometer for identifying charged particles and measuring their momenta. Electrons/positrons and charged hadrons (pions, kaons, protons, and heavier nuclear fragments) are identified by measuring the particle's time of flight between the start detector located ahead of the target and two systems of scintillation hodoscopes installed behind the magnet. TOFINO, one of these systems (see Fig. 1), covers a region of polar angles from 18° to 45° and is comprised of 24 radial scintillation detectors grouped by four detectors in each of the six sectors. The scintillation tile of each detector has a 1-cm-thickness and a trapezoidal shape with a height of ~130 cm and bases of 12 and 32 cm. A light guide composed of 32 specially bent plastic plates with a square (1×1 cm^2) cross section collects light from the larger tile base onto XP2020 and Hamamatsu 1949 photomultiplier tubes (PMTs). The time resolution of this system is ~450 ps. The TOFINO system was used in a number of the first experiments at the HADES setup to study hadron–hadron and proton–nucleus interactions, as well as in the experiments on collisions of light nuclei, in which the probability of two or more particles hitting the same scintillation detector in a single event, was substantially less than unity. For use in experiments on studying collisions of heavy nuclei, the TOFINO system was replaced with a higher-granularity system based on resistive plate chambers (RPCs) [4]. Preliminary results of analysis of Au + Au

reaction data at 1.24 GeV/nucleon have shown that the new RPC system exhibits time resolution $\sigma \approx 80$ ps.

The other scintillation hodoscope of the time-of-flight (TOF) system [5] covers the range of polar angles from 45° to 88°. It consists of 384 scintillation detectors also divided into six sectors. The length of a scintillation tile increases with an increase in the polar angle. The square cross section of each tile is 2×2 cm^2 for the inner 192 tiles and 3×3 cm^2 for the farthest 192 tiles. Such geometry provides a high degree of granularity in the polar angle range of 45°–88°, thus reducing the probability of particles doubly hitting the same tile in a single event even in reactions with heavy nuclei. The light from both ends of each scintillation tile is collected to an EMI9133B PMT by means of plastic light guides. The time resolution of this scintillation hodoscope is $\sigma \approx 180$ ps.

Along with the TOF system described above, the threshold ring-imaging Cherenkov detector (RICH) is used to identify electrons. The RICH is located in the region around the target, where the magnetic field is absent. In addition, the pre-shower detector is also used for this purpose in the region of forward angles. The RICH identifies leptons, being insensitive to fast pions with energies as high as 3 GeV, and the pre-shower detector helps improve discrimination between leptons and hadrons based on the method of detecting an electromagnetic shower produced by electrons.

The momenta of charged particles and the angles of their exit from the target are measured by the tracking system of detectors composed of a superconducting toroidal magnet and four planes of mini-drift chambers (MDCs). The chambers measure the position and direction of charged particles before and after the magnetic field region. The momentum of each particle is determined by the bending of particle paths in the magnet. This system exhibits the momentum resolution for charged particles of ~1%.

The two-level trigger system is used to select events. It allows selection of events by their central position using information on the particle multiplicity in the TOF system, as well as by online identification of leptons in the RICH, TOF, and pre-shower detector subsystems. This selection helps reduce the quantity of background events and the amount of data saved to a hard disk. The HADES detector systems, the organization of the trigger, the data acquisition system, and data analysis were described in detail in [3].

The forward multichannel scintillation hodoscope called the Forward Wall (FW) is one more important detector system of the HADES setup (see Fig. 1). The forward hodoscope was used for the first time to study the production of electron–positron pairs in *np* interactions at a 1.25-GeV energy of incident neutrons [6]. The hodoscope was located at a distance of 7 m behind the target downstream of the beam and covered the polar angle region between 0.33° and 7.17°. A deuteron beam was used in the experiment as the bombarding beam, and the target was made of liquid hydrogen. The method for identifying the *np* reaction consisted in detecting a spectator proton from a deuteron nucleus by the forward hodoscope. After the substantial upgrading of the electronics, the FW was used for the first time in the experiment on studying electron–positron pair production in the Au + Au reaction at 1.24-GeV/nucleon energy of bombarding Au nuclei. In this experiment, the maim function of the forward hodoscope was to determine the reaction plane in event-by-event data analysis and to use data obtained thereby to analyze charged particle fluxes.

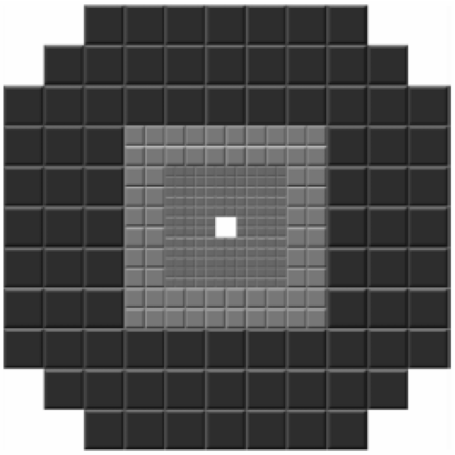

Fig. 2. Arrangement of the scintillating detector cells in the forward hodoscope of the HADES setup.

3. DESIGN AND PERFORMANCE CHARACTERISTICS OF THE FORWARD HODOSCOPE

The forward hodoscope of the HADES setup is a 288-channel system of scintillation cells for detecting charged particles. The diagram of the arrangement of detector cells in the forward hodoscope is presented in Fig. 2. The symmetrical geometry of the scintillation cell arrangement has been selected to optimize the acceptance and reduce the contribution of systematic errors to the determination of the reaction plane angle.

The forward hodoscope consists of 140 scintillation detector cells located in the central region, 64 cells in the middle region, and 84 cells in the outer region. The detector cells used in the central hodoscope region are small-sized (scintillators with an active area of 4×4 cm^2), the cells in the middle region are medium-sized (scintillators with an active area of 8×8 cm^2), and, finally, the cells in the outer region are large (scintillators with an active area of 16×16 cm^2). The thickness of all scintillating detector cells is 2.54 cm. The radiations are made of BC408 polystyrene-based plastic scintillators. There is a hole with a cross section of 8×8 cm^2 at the geometrical center (downstream of the beam) of the forward hodoscope for transmitting the primary beam of relativistic particles. The total transverse

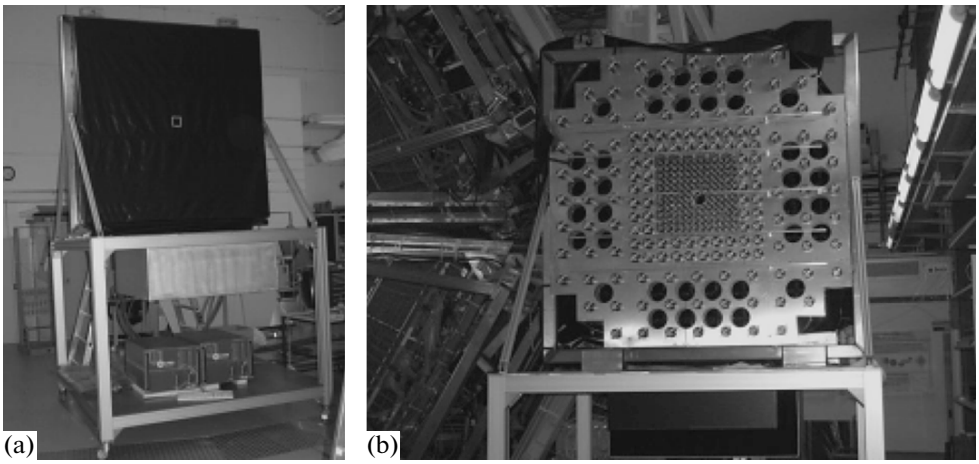

Fig. 3. (a) Frontal view of the forward hodoscope (covered with a protective film) and (b) view from the rear side of the forward hodoscope with holes for mounting the PMT cases.

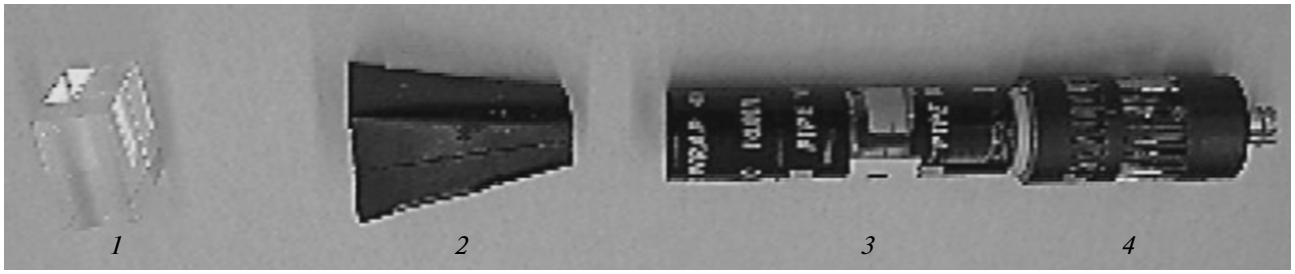

Fig. 4. Functional elements of the scintillating detector cells in the forward hodoscope: (*1*) BC408 scintillator, (*2*) air light guide, (*3*) XP2982 and XP2262 PMTs, and (*4*) HV divider.

dimensions of the forward hodoscope are 180 × 180 cm. The scintillation detectors from the forward hodoscope of the KaoS setup (GSI, Darmstadt) have found application in our hodoscope [7].

Figure 3a shows a photo of the forward hodoscope's front side covered with a light-insulating film and the high-voltage (HV) supply modules on a mobile platform in the experimental room of the HADES setup. The photo in Fig. 3b demonstrates the general view of the back side of the forward hodoscope with easily discernible holes for mounting PMT cases.

An individual scintillation detector cell of the forward hodoscope consists of the following functional components (Fig. 4):

—a BC408 plastic scintillator;

—an air light guide that has a casing made of an aluminum alloy with a polished light-reflecting inner surface and is used to collect light from the scintillator onto the PMT photocathode;

—an XP2982 PMT for small-sized detector cells at the center of the forward hodoscope and an XP2262 PMT for medium- and large-sized detector cells in the intermediate and outer hodoscope regions; and

—HV dividers of the PMT bias.

The main parameters of the XP2982 and XP2262 PMTs are presented in the table.

Since the number of photons produced by a detected particle in scintillation cells of the forward hodoscope is proportional to the particle charge squared, measurements both of spectator protons and of heavy multicharged fragments must be taken over a wide dynamic range of the output signal amplitude. For the dynamic range to be reduced, the used HV dividers of the PMT bias ensure a decrease in the dynode voltages and, hence, a decrease in the PMT gain in proportion to the current in the dynode system. Owing to this design of the dividers, the linear depen-

Main parameters of the XP2982 and XP2262 PMTs

PMT type	Current pulse rise time, ns	Number of dynode stages	Photocathode diameter, mm
XP2982	1.9	11	29
XP2262	2.0	12	51

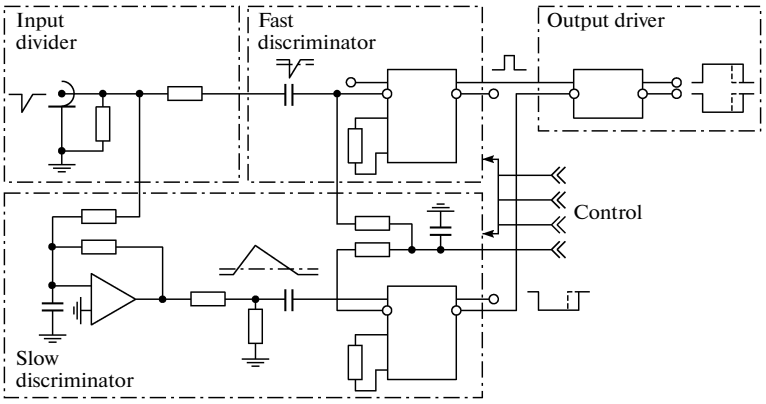

Fig. 5. Simplified diagram of the TOFAddOn analog signal processing module implementing the time-to-pulse conversion method.

dence of the output signal amplitude on the charge of a detected fragment is attained.

4. READOUT ELECTRONICS FOR THE FORWARD HODOSCOPE DETECTORS

The data acquisition system unified with the TOF detector of the HADES setup was used to read out the PMT signals in the scintillation cells of the forward hodoscope. This is a distributed system (crate modules are not used in it) based on a single system module—Trigger Readout Board (TRB)—at all levels of the data acquisition system hierarchy [8]. At the lower level, a TOFAddOn 128-channel analog module of amplifiers–discriminators corresponds to each TRB module. In this case, the TOFAddOn analog module is fully controlled, powered, and read out by the TRB module. Therefore, integrating the TRB and TOFAddOn modules in a single unit, one obtains the minimal and self-containing component of the data acquisition systems with 128 readout channels.

The TOFAddOn analog signal processing module was developed especially for the TOF detectors of the HADES experiment in combination with the TRB system module. The TRB module contains four high performance time-to-digital converter (HPTDC) chips (CERN, ALICE) [9] with a 100-ps time resolution (the rms deviation is 40 ps). In this case, the time-to-digital converters operate in the so-called multi-hit mode, thus providing a means for measuring both the arrival time of the pulse leading edge and the pulse duration (calculated as the difference of the leading and trailing edges of a pulse), which corresponds under certain conditions to the input charge value. The pulse duration range specified by the 100-ps resolution and 12-bit HPTDC time-to-digital converters is 4096×100 (ps) $\approx$ 400 ns.

The concept of the time-to-pulse conversion (TPC) was used in designing the TOFAddOn 128-channel analog signal processing module. The simplified circuit diagram of the discriminator is shown in Fig. 5.

To ensure the unambiguous correspondence of the input charge to the pulse duration, a two-threshold discriminator structure has been selected for the TOFAddOn module. The leading and trailing edges of the output pulse from the circuit are formed by the fast and slow discriminator channels, respectively. This circuit design ensures the precise timing by the leading edge (with an inherent time jitter of <10 ps), as well as the correspondence of the pulse duration to the input charge with an accuracy of ~0.3%.

Both discriminators are based on an 8-channel dedicated NINO chip [10], which has been developed by the CERN especially for TOF systems in the ALICE experiment. The fast discriminator has no features, except for the time expansion function implemented by adding a constant value to the pulse duration. Similar time expansion has also been introduced to the slow discriminator to exclude generation of doubled pulses in one event. The separate setting of the thresholds and additional durations for the fast and slow discriminator channels makes it possible not only to tune the discriminator for operation with a particular input pulse waveform, but also to obtain an unambiguous dependence of the charge on the pulse duration. The results of the TPC discriminator testing using a 7-ns-long signal from a pulse generator are shown in Fig. 6. From Fig. 6, it is apparent that this dependence becomes linear starting with a signal amplitude of 500 mV. This is attained by introducing a forcible amplitude limitation mode in the slow discriminator channel. As a result, the increment of the duration in the analog stage with a strictly limited amplitude proceeds linearly, since it obeys the charge conservation law. The accuracy of the measurable quantity, calculated as the ratio of the rms deviation of the pulse duration to its averaged value at each point, is presented in square brackets.

The feature of the slow discriminator channel is the use of a special analog stage producing the output

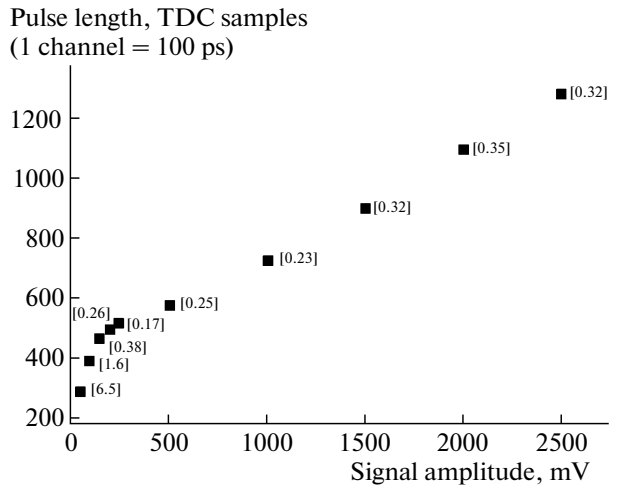

Fig. 6. Duration of the TPC discriminator pulse as a function of the signal amplitude from the pulse generator. The uncertainty of the measured value (see text) is given in square brackets.

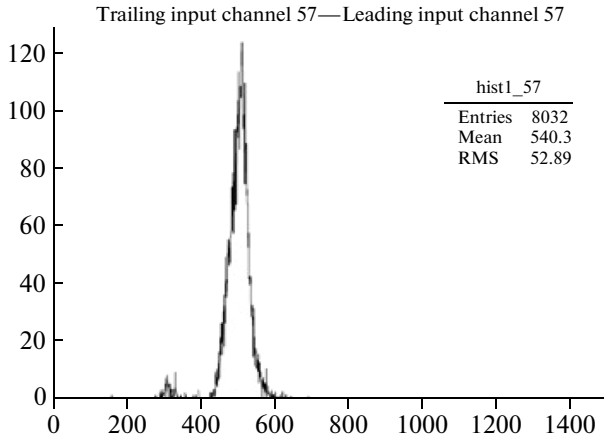

Fig. 7. Threshold artifact in the region of the 300th TDC channel in a typical charge spectrum of the TPC discriminator. The TDC channels are laid on the horizontal scale with a scale division value of 100 ps, and the samples are laid on the vertical scale.

pulse with an invariable shape the amplitude of which is proportional to the charge integrated on the time interval of ~30 ns. This stage is a matter of principle for the correct reconstruction of the charge from the pulse duration, since the TPC method practically implies scanning of the varying signal waveform with a constant threshold.

The presence of a small (~1% of the efficiency) peak in the charge spectrum (the "threshold artifact") is a criterion of correct circuit tuning (Fig. 7). This peak must be located precisely at the threshold of action of the fast discriminator, which corresponds to the 300th channel of the TDC samples (30 ns). The presence of this peak indicates that the fast discriminator is triggered before the slow one; i.e., the timing accuracy is not "smeared" by the operation of the slow discriminator channel. As the results of measurements show, it is impossible to eliminate the threshold artifact, since it is originated by the dynamic nonuniformity of the PMT output pulse waveform at a constant amplitude.

Control over the digital interface between the TRB and TOFAddOn modules provides a means for programmatically setting the common (for all the 128 channels) and individual thresholds of the fast and slow discriminators, the output signal lengths, and the hysteresis value. The range of the pulse lengths at the TOFAddOn module output varies from the minimum value of 30–40 ns (the length at the discriminator threshold is specified programmatically) to 400 ns (the TDC range boundary), which is determined by the invariable parameters of the analog part in the slow discriminator circuit.

5. TUNING AND CALIBRATION OF THE FORWARD HODOSCOPE

5.1. Equalizing the Amplitude Response of Hodoscope Detector Cells Using Cosmic Rays

Identification of noninteracting nuclear fragments in the forward hodoscope requires the wide dynamic range of the amplitude scale in recording of output signals from each individual detector cell. In fact, the energy deposited in the scintillator by fragments with charge $Z = 10$ must be 100 times higher than the energy deposited by a proton with $Z = 1$. As noted in Section 3, for the dynamic range to be reduced, the HV dividers of the PMT bias ensure the voltage drop across the dynodes proportional to the current in the dynode system. Owing to this design of the HV dividers, the dependence of the signal amplitude on the charge of a detected fragment is linear. Further optimization of the dynamic range of the amplitude scale is effected by tuning the PMT gain. It is apparent that the amplitude peak due to charged particles with $Z = 1$ should be located on the amplitude scale as close to the pedestal as possible, but, incidentally, be reliably distinguished from the spectrum of low-energy particles with a peak located also near the pedestal. This peak in the region of the 550th channel can be attributed to the nonlinearity of the TOFAddOn module response observed in this region (see Fig. 6).

The PMT gains were tuned using cosmic rays before the set of measurements on the ion beam. A trigger was organized for this purpose, which requires activation of at least five scintillating hodoscope cells. As a result, the trigger selected cosmic muons passing predominantly in the vertical plane (the hodoscope plane). The energy deposited by cosmic muons (and, as result, the number of produced photons) is known to be proportional to the muon

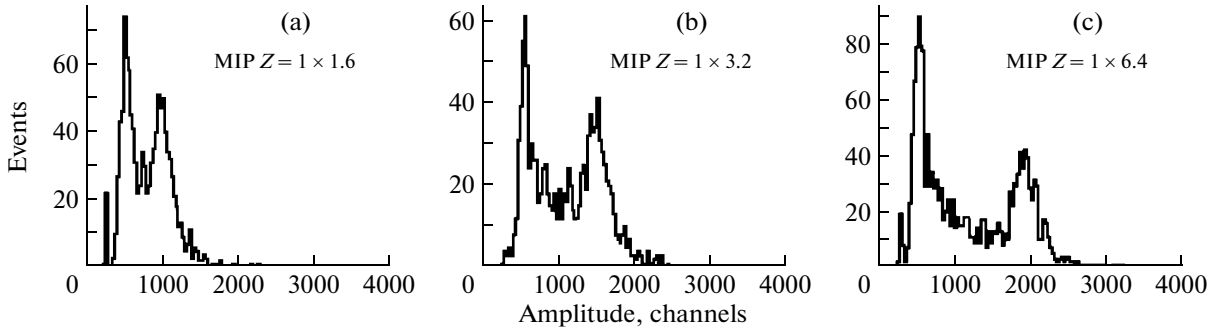

Fig. 8. Amplitude spectra from cosmic muons that passed through (a) the central, (b) middle, and (c) outer detector cells of the forward hodoscope. The first peak in the histograms corresponds to the pedestal and the second peak is due to muons with low deposited energies, i.e., minimum ionizing particles (MIPs). The values of parameter Z correspond to the ratio of the transverse cell dimensions to the cell thickness downstream of the beam.

range in a scintillator and, for the forward hodoscope, depends on the transverse dimensions of the central, middle, and outer detector cells. The amplitude spectra of cosmic muons in detector cells of different types are presented in Fig. 8. The left narrow peak in Fig. 8 corresponds to the pedestal. The middle peak in the 550th channel corresponds to low energies deposited by muons. The right peak corresponds to the energy deposited by vertical muons that passed through the entire cell. From Fig. 8, it is apparent that the peak amplitudes are proportional to the transverse dimensions of the detector cell.

The accuracy of PMT gain tuning is illustrated by Fig. 9, which shows the amplitude spectra from ion fragments that passed through the central, middle, and outer detector cells of the forward hodoscope in the Au + Au reaction at an energy of 1.24 GeV/nucleon. From the figure, it is evident that the position of the peak corresponding to the energy deposited by particles with $Z = 1$ in detector cells of all types is approximately the same and corresponds to the ≈900th channel.

Therefore, the use of the special trigger for the selection of cosmic muons in the vertical plane has made it possible to equalize the PMT gains and optimize the dynamic range of the amplitude scale for the forward hodoscope cells immediately before the set of measurements.

5.2. Time Calibration of the Hodoscope Detector Cells on the Beam

The time calibration is aimed at determining the coefficients of conversion of the fast discriminator response time in terms of the channel number to the TOF of the spectator particle from the target to the respective detector cell of the forward hodoscope in terms of nanoseconds. The calibration procedure was individually performed for each hodoscope cell.

In the first phase, the time correction parameters due to the time–amplitude dependence of the signal from the detector cell were determined. This correction was based on the formula $t = a_1 + a_2/\sqrt{ADC}$, where t [ns] is the corrected time, a_1 and a_2 are the parameters of the time–amplitude dependence fit, and *ADC* [channels] is the signal amplitude. Figure 10 presents the time–amplitude dependences of the signals in a small (central) cell of the forward hodoscope before and after the application of the time–amplitude correction procedure. Execution of this procedure results in a weaker dependence of the spectator's TOF on the signal amplitude in the forward hodoscope cell (see Fig. 10, on the right).

In the second phase, the time spectrum offset was calculated so that the TOF of the spectator particle became equal to the theoretical value of its TOF from the target to the calibrated detector cell. For a particular momentum of the spectator particle, this time depends only on the distance from the target to the center of the respective hodoscope cell. The TOF spectrum of the calibrated cell after the time–amplitude correction and the TOF spectrum reduced to the theoretical value for this cell are shown in Fig. 11.

After all the detector cells of the forward hodoscope were calibrated, the resolution was estimated by the TOF of spectator particles for individual cells, and the total resolution was estimated by the TOF for cells of each size. As an example, Fig. 12 presents the TOF distributions for isolated cells of three different sizes, and Fig. 13 shows the total TOF distributions for the small, medium, and large detector cells.

From these distributions, it is apparent that the best time resolution of ~690 ps is exhibited by the small hodoscope cells, whereas, for the medium and large cells, the time resolution is ~700 and ~930 ps, respectively. This resolution is fully sufficient for the identification of spectator particles having a 25-ns TOF in this reaction.

The stability of the time calibration parameters was tested using data acquired over the whole set of measurements (26 days) of the Au + Au reaction at an energy of 1.24 GeV/nucleon. The mean TOF values of spectators to different hodoscope detector cells are

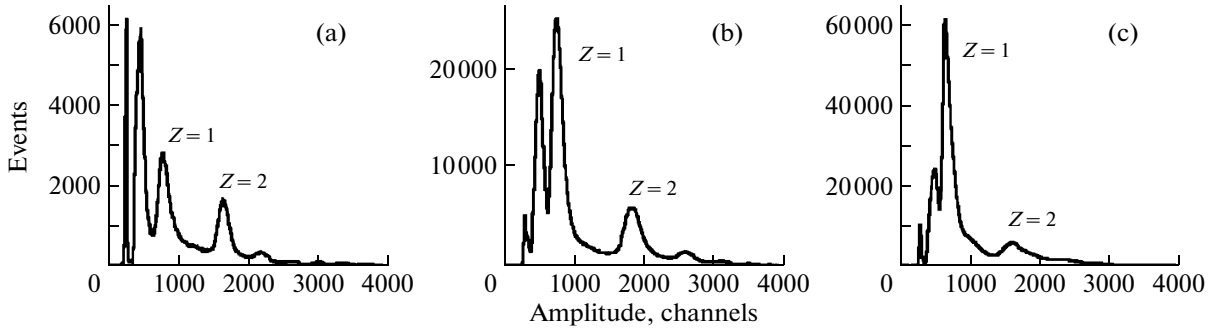

Fig. 9. Amplitude spectra from beam ion fragments that passed through (a) the central, (b) middle, and (c) outer detector cells. The first peak in the histograms corresponds to the pedestal and the second peak is due to MIPs.

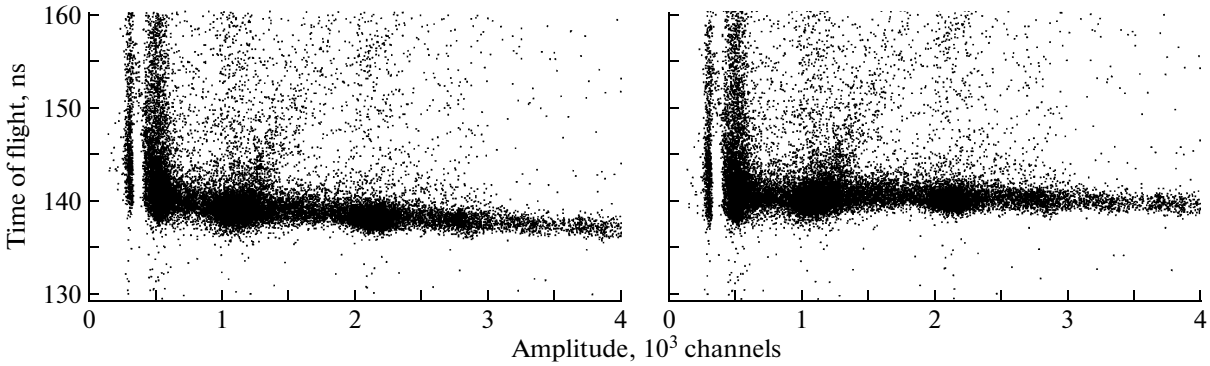

Fig. 10. Time–amplitude dependence of the signals in one of the small (central) cells of the forward hodoscope before (on the left) and after (on the right) the time–amplitude correction procedure is applied.

presented in Fig. 14 as a function of the measurement time. These data allow one to estimate the quality of the time calibration of the forward hodoscope.

5.3. Amplitude Calibration of the Hodoscope Detector Cells on the Beam

Apart from determining the TOF of spectators from the target to the respective detector cell in the forward hodoscope, their electric charge must also be measured to identify spectator particles detected by the forward hodoscope. For this purpose, the energy losses of spectators were measured in the scintillating cells of the forward hodoscope, which were proportional to the square of the detected particle charge. However, as noted above, the used PMT voltage dividers maintained the drop of the dynode voltages such that it was proportional to the current in the dynode system. This design of the dividers allowed the linear dependence of the signal amplitude on the electric charge of a detected spectator particle to be attained and the dynamic range of the amplitude scale to be reduced. The PMT gains were selected in the test experiments on cosmic rays so that the amplitude peak from charged particles with $Z = 1$, on the one hand, was located as close as possible to the pedestal and, on the other, was reliably separated from the spectrum of low-energy particles with a peak near the pedestal (≈550 th channel). As noted above, this peak can be attributed to the nonlinearity of the TOFAddOn response (see Fig. 6).

The typical shape of the spectra characteristic of the small (located near the beam axis), medium (located at a distance from the beam center), and large (located at the periphery) hodoscope detector cells is shown in Fig. 15.

The amplitude scale of each hodoscope detector cell was calibrated for subsequent data analysis. The calibration consisted in equalizing the peak positions on the amplitude scale for spectators with a fixed charge for all hodoscope detector cells. Taking into account the linear dependence of the signal amplitude on the charge of a detected spectator particle, the calibration was reduced to linear transformation, which resulted in setting the two first peaks for spectator particles with electric charges $Z = 1$ and 2 in fixed positions on the calibrated amplitude scale. In this case, it may be expected that, after making this calibration, peaks in the spectra of spectator particles with high electric charges will be located with a high precision in

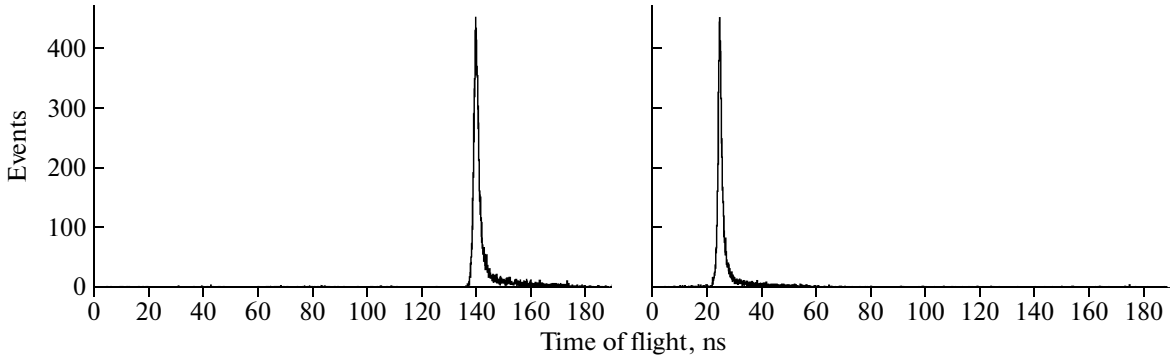

Fig. 11. Time spectrum after the application of the time–amplitude correction procedure (on the left) and time-of-flight spectrum set at the theoretical value (on the right) for small (central) detector cell no. 51 in the forward hodoscope.

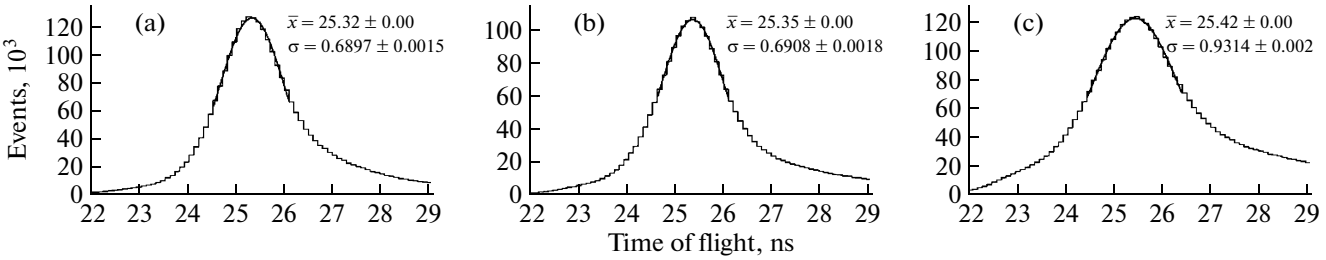

Fig. 12. Spectator time-of-flight distributions (a) for the central, (b) middle, and (c) outer detector cells of the forward hodoscope.

the same positions for all detector cells of the forward hodoscope. Since the two first spectrum peaks (on the left of the 750th channel) presented in Fig. 15 by way of example are not of the physical nature and result from peculiarities of the electronic system (the first peak corresponds to the pedestal, and the second is due to the TOFAddOn nonlinearity, as noted above), they have not been subjected to further processing and correction. The calibration of the amplitude scale was thereby performed for the third and fourth peaks (Fig. 15).

In order to automate the calibration process, the positions of the maxima corresponding to the spectator particle charges equal to 1 and 2 were determined. To do this, each distribution was preliminarily smoothed by the median filter with a kernel of 5 to eliminate noise and more precisely determine the peak positions (Fig. 16). This processing allows us to determine the number of peaks by simple counting. For the peak positions to be refined, the initial spectrum shape was fitted with the Gaussian distribution.

This algorithm offers a chance to find from 2 to 15 peaks in the amplitude spectrum if the data acquisition time was a few hours. Note that >90% of all cells have >2 peaks (Fig. 17), which is sufficient for making the above-described calibration.

After this, a linear transformation was performed, as a result of which the read signal amplitudes were mapped onto the calibrated scale. To do this, a value of

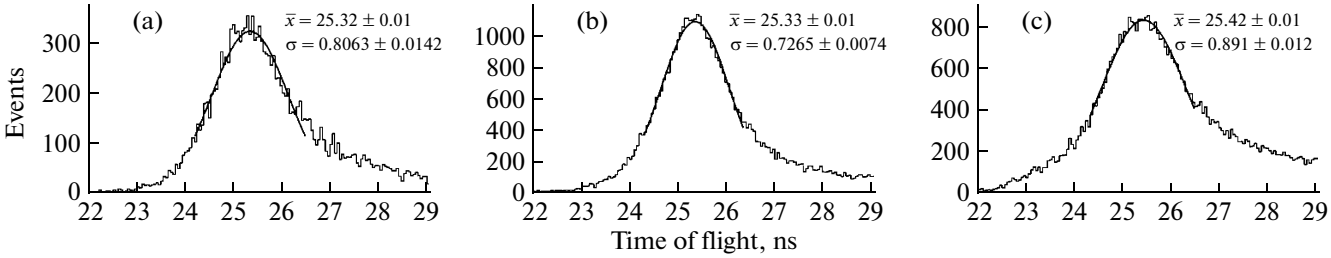

Fig. 13. Total distributions in the spectator time-of-flight (a) for the central, (b) middle, and (c) outer detector cells of the forward hodoscope.

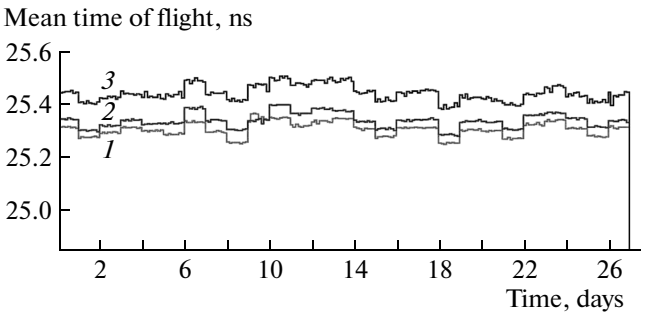

Fig. 14. Mean spectator time-of-flight values (*1*) for the central, (*2*) middle, and (*3*) outer detector cells of the forward hodoscope vs. the measurement time.

100 arbitrary units was assigned to the amplitude peak corresponding to the unit electric charge of the spectator, and 200 arbitrary units of the calibrated scale were assigned to the charge of 2 units. To verify the hypothesis of correct finding of the maxima, it was necessary that the position of the third peak (the charge was equal to 3) on the scale after its calibration be the same for all cells with a high degree of accuracy.

As a result, parameters a and b of the linear transformation $E = aE' + b$ were obtained for each hodoscope cell, where E' is the read signal amplitude, and E is the signal amplitude calibrated in terms of arbitrary units. The result of the calibration is presented in Fig. 18. From Fig. 18, it is apparent that the selection of the linear transformation for calibrating the scale with the aim of leveling the peaks in the amplitude spectrum is justified.

After this calibration, one can, with a high degree of accuracy, specify the boundaries of amplitude peaks at levels independent of the detector cell number in the forward hodoscope. Significant deviations have been noted beginning with the forth peak, which is sufficient for the first phase of the physical data analysis. If further analysis requires the relative coincidence of all peak positions for different detector cells, there is a chance to use piecewise-linear transformation between the values of all recorded peaks or to limit oneself to tabulation of individually selected boundaries.

The investigation of the long-term stability of the amplitude peak positions for different detector cells has demonstrated that, for the overwhelming majority of cells, there is a small deviation of their positions from the initial values on the average by ≈3% over the time of the physical measurement (about 20 days). This fact is illustrated by Fig. 19, which shows the position of the amplitude peak for $Z = 1$ in one of the forward hodoscope cells during the physical measurement.

Using an individual set of calibration factors for each period of time, one can attain the stable position of the peaks and correct thereby the time drift. The data of the amplitude calibration for each detector cell and for each day of the physical measurement are saved in the database and are available for analysis.

6. USE OF THE FORWARD HODOSCOPE IN THE EXPERIMENT ON STUDYING THE YIELD OF DILEPTON PAIRS IN NEUTRON–PROTON INTERACTIONS AT THE HADES SETUP

The forward hodoscope has been used for the first time at the HADES setup in the experiment on studying the dilepton yields in the reaction of interaction between bombarding 1.25-GeV quasi-free neutrons and protons of a liquid-hydrogen target (2007). By that time, the first statistical data of the DLS experiment have already been available [2]. In these data, a substantial excess was observed in the yield of electron–positron pairs over the expected total contribution from hadron decays detected in collisions of carbon nuclei at an energy of 1 GeV/nucleon. Various theoretical models were incapable of explaining the observed discrepancy for about two decades. Thus, the data of the DLS experiment, remaining unexplained

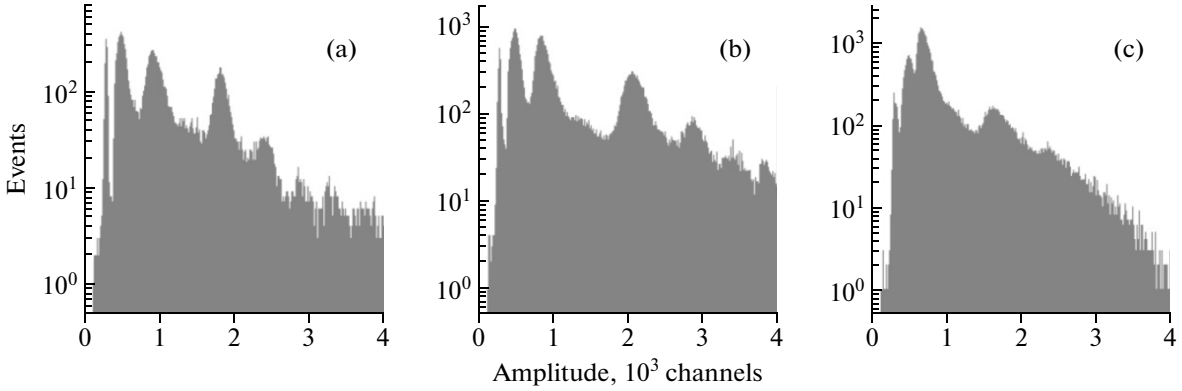

Fig. 15. Examples of the amplitude spectra of the energies deposited (a) in the central, (b) middle, and (c) outer cells of the forward hodoscope.

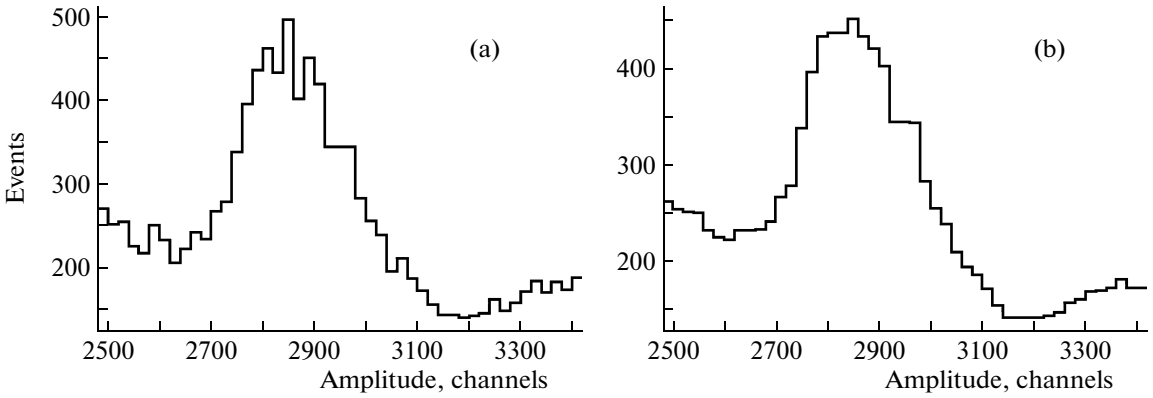

Fig. 16. Third peak in the amplitude distribution for detector cell no. 160 (a) before and (b) after the application of the median filter.

for a long period of time, have initiated the development of the whole subsequent program of dilepton measurements in nucleus–nucleus collisions. In the first experiments at the HADES setup in the early 2000s, the dielectron yields were measured in the carbon–carbon system at beam energies of 1 and 2 GeV/nucleon [11]. It should be noted that the HADES is better in the engineering aspect than the setup used in the DLS experiment. Apart from the substantially higher mass resolution (~2% for the HADES against ~10% for the DLS), the acceptance of the HADES exceeds that of the DLS by a factor of ~10. As was the case with the DLS experiment, the HADES collaboration also revealed the excess of the dielectron yield over the expected total contribution of hadron decays. Comparing the spectra of the invariant masses and the transverse momenta obtained with the HADES setup and referred to the DLS acceptance, one can see that the data are in good agreement. Therefore, any doubts about the reliability of the experimental data obtained by the DLS collaboration have been removed.

Nevertheless, the question about possible causes of the increase in the yield of electron–positron pairs in collisions of carbon nuclei at an energy of 1 GeV/nucleon has remained open. The assumption arose that the incorrect inclusion of the dielectron production processes in elementary nucleon–nucleon collisions might be responsible for the observed enhancement of the electron–positron pair yield. In 2006, the HADES collaboration performed measurements of the electron–positron pair yield in proton–proton collisions at an incident proton energy of 1.25 GeV [12]. There were no experimental data in the neutron–proton channel, and obtaining them was a matter of considerable interest. It should be noted that a significant role in this channel was predicted for the bremsstrahlung process, which was inadequately investigated in the theoretical aspect.

An experimental run of deuteron–proton collisions was performed in May 2007 to study the yield of electron–positron pairs in interactions between bombarding neutrons and target protons. The deuteron beam with an energy of 1.25 GeV/nucleon and an intensity of 10^7 particles/s was incident on the liquid hydrogen target with a length of 5 cm and a thickness of 0.35 g/cm^2. The deuteron beam acted as a neutron source in this experiment. In the context of the momentum approximation, a collision of a high-energy deuteron with a target nucleon can actually be considered as the quasi-free nucleon–nucleon interaction. In this case, a nucleon contained in a deuteron that does not participate in the reaction is considered to be the spectator particle. Therefore, if a proton from the incident deuteron nucleus does not take part in the interaction with the target proton and is identified by the forward hodoscope as a spectator proton, it is possible to identify the reaction of interaction between the neutron included in the deuteron nucleus and the target proton. To do this, the trigger of the first level in this experiment selected events having ≥2 charged particles in the system of TOF measurements by the TOF and TOFINO detectors in coincidence with detection of ≥1 charged particle in the forward hodoscope.

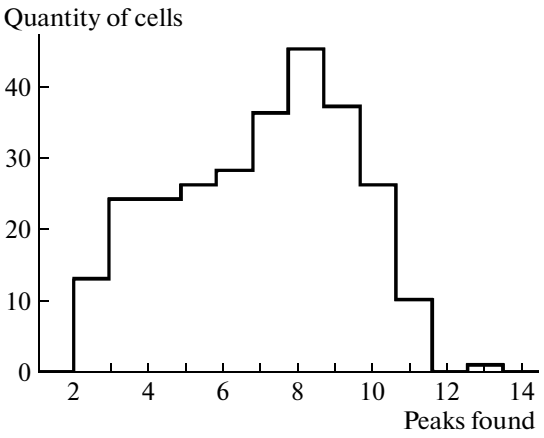

Fig. 17. Number of automatically found peaks in the amplitude spectra for all hodoscope detector cells.

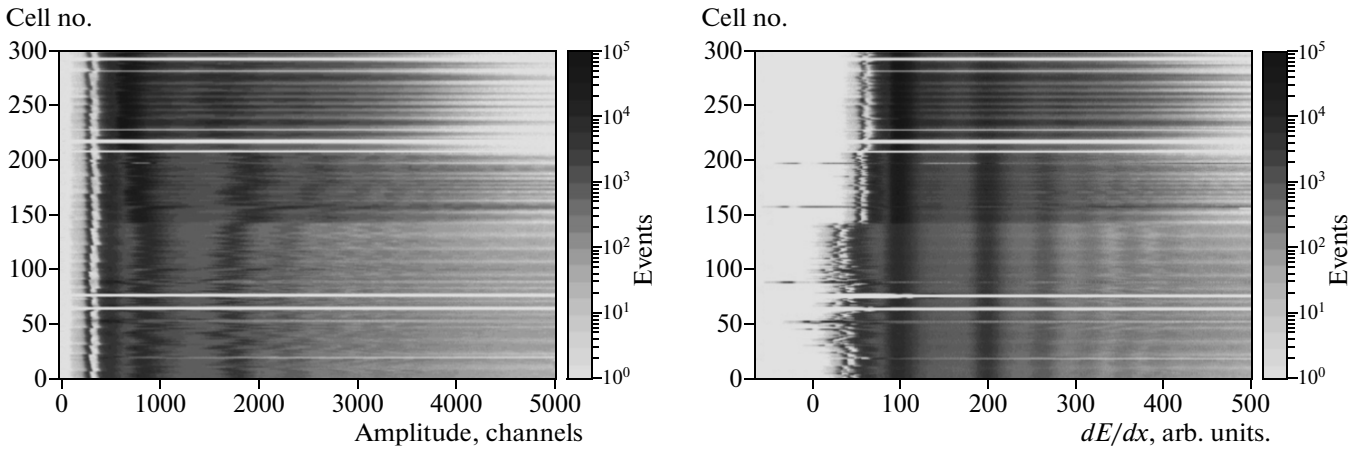

Fig. 18. Distribution of energies deposited by spectators in the scintillating cells of the forward hodoscope according to the cell numbers before (on the left) and after the calibration (on the right).

In this experiment, the forward hodoscope was set at a distance of 7 m from the target and covered the polar angle range of 0.33°–7.17°. The forward hodoscope measured the coordinate of a charged particle (the coordinate of the center of the appropriate hodoscope detector cell which the particle hit), the TOF, and the signal amplitude from the appropriate hodoscope cell carrying information on the energy losses of the incident charged particle.

Since there is no magnetic field in the above range of polar angles, it is impossible to directly measure the particle momentum (and, hence, identify its type). Simulation has demonstrated that spectator protons dominate in the angular range covered by the forward hodoscope and that the major portion of them hit the central part of the hodoscope with the smallest detector cells and, hence, with the best time resolution. The simulation has also shown that a fraction of spectator protons incident on the forward hodoscope is ~90%. In this case, the highest quantitative losses of them can be attributed to the presence of a central hole for passing of the beam particles. Therefore, the forward hodoscope detects the overwhelming majority of spectator protons.

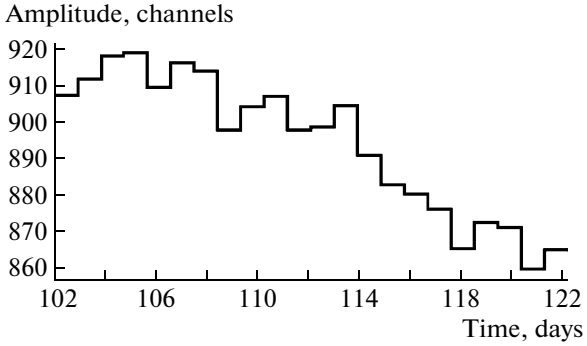

Fig. 19. Peak position for $Z = 1$ on the amplitude scale for detector cell no. 60 during the set of physical measurements.

When determining the momentum of a detected particle, any detected charged particle was assumed to be a proton. Therefore, the particle momentum can be determined by the measured particle flight time from the target to the appropriate hodoscope detector cell. The accuracy in determining the particle momentum is governed by the time resolution of the hodoscope cells. The spectator proton momentum should be approximately one-half the beam momentum. For a deuteron beam with an energy of 1.25 GeV/nucleon, this value is 1.97 GeV/c.

To discriminate between the channels of neutron–proton and proton–proton collisions, constraints were imposed on the reconstructed momentum of the detected charged particle under the assumption that the detected particle was a proton. For proton–proton collisions, the reaction protons had kinetic energies of <1.25 GeV (or momenta of <1.97 GeV/c). The momentum distribution of particles detected in the forward hodoscope both in proton–proton and neutron–proton reactions is presented in Fig. 20. It is clearly seen that the fraction of proton–proton collisions is rather small even in the absence of constraints on the momentum in the forward hodoscope. Nevertheless, the wide momentum range of $1.6 < p < 2.6$ GeV/c has been selected for identification of the neutron–proton channel.

The upper boundary helps remove light particles with very high values of the reconstructed momentum (e.g., electrons, positrons, and γ-ray photons, which can be detected by the forward hodoscope with a low efficiency). The limitation on the minimum momentum was set by optimizing acceptances for the neutron–proton and proton–proton reactions and the fraction of each reaction type in the total spectrum of electron–positron pairs versus the lower limit on the momentum. A comprehensive investigation of these

questions, as well as the experimental verification of the applicability of the momentum approximation criteria for extracting the reaction of quasi-free neutron–proton interaction, was described in detail in [13].

7. USE OF THE FORWARD HODOSCOPE TO DETERMINE THE (Au–Au) REACTION PLANE ANGLE

One of the important aims of the experiments performed at the HADES setup is to study collective flows of charged particles in semi-central collisions of heavy nuclei, which manifest themselves as the azimuthal anisotropy of the momentum distribution of produced charged particles. The azimuthal anisotropy in the momentum space results from the fact that, in semi-central nuclear collisions, the region of overlap of colliding nuclei in the coordinate space is an ellipsoid of revolution, inside which secondary particles are produced in interactions between particles of a bombarding and target nuclei. This spatial anisotropy of the region of interaction of colliding nuclei results in the fact that pressure gradients are generated during thermalization of the produced matter. In this case, the pressure reaches its maximum along the minor axis of the ellipsoid and its minimum along the major axis. As a result, the azimuthal momentum distribution of particles becomes anisotropic. In experiments, the anisotropy in the momentum distribution of escaping charged particles produced thereby is investigated relative to the so-called reaction plane, which is determined by the axis of the incident beam and the vector connecting the centers of colliding nuclei.

In the experiments at the HADES setup, the secondary particle spectra are measured by the magnetic spectrometer in the polar angle range of 18°–88°. The hodoscope described above is used to determine the reaction plane angle in the laboratory coordinate system. It identifies charged fragments–spectators of an incident nucleus, i.e., particles that do not take part in the interaction and carry information on the centrality of the interaction: the closer to the center the interaction, the fewer spectators hit the forward hodoscope.

The sphericity tensor method [14] and the total transverse momentum transfer technique [15] have been developed and used to determine the reaction plane angle in experimental studies of nucleus–nucleus interactions. Since the forward hodoscope of the HADES setup is incapable of measuring the transverse momentum of spectators, the modified total transverse momentum transfer technique [16, 17] has been used in our study. According to this technique, the reaction plane is determined in each event by the direction of the incident beam and vector $\vec{Q}$, which is equal to the sum of the weighted transverse velocity vectors of all charged fragments–spectator in this event. Therefore, azimuthal reaction plane angle φ_{RP} is the angle between axis $0X$ and vector $\vec{Q}$.

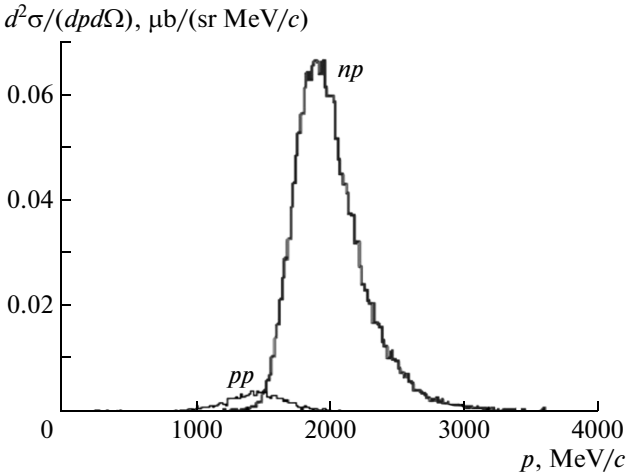

Fig. 20. Spectrum of proton pulses detected in the forward hodoscope: (*pp*) contributions of proton–proton interactions (the spectrum in the momentum range of 1000–2000 MeV/c), and (*np*) contributions of neutron–proton interactions (the spectrum in the momentum range of 1400–3200 MeV/c).

The distinctive feature of spectators of an incident nucleus is the equality of their velocities, regardless of the spectator mass. Therefore, the transverse velocity vectors of the spectators are oriented in parallel to the respective spatial vectors of the spectator positions in the (X, Y) plane perpendicular to the beam axis, i.e., in the plane of the forward hodoscope. Vector $\vec{Q}$ can be presented in the form

$$\vec{Q} = \sum_{k=1}^{M} \omega_k \vec{r}_k / |\vec{r}_k|, \qquad (1)$$

where M is the number of cells triggered in an event satisfying the spectator criteria, $\vec{r}_k/|\vec{r}_k|$ is the unit vector of the kth hodoscope cell position in the event, ω_k is the weight dependent on the spectator rapidity and its transverse momentum, and the sign of ω_k is positive for particles flying forward in the center-of-mass system and negative for particles flying backward. The weight value is selected for the reasons of the best angular resolution for the reconstructed orientation of the reaction plane; nevertheless, regardless of the selection, the weight value affects the obtained angular resolution only slightly. If the detector is incapable of measuring the transverse particle momentum, the absolute value of the weight may be selected equal to unity [16, 18]. For the scintillation forward hodoscope measuring the spectator charge, the selection of the weight value equal to the spectator charge provides better results in comparison with the unit weight [17], which is corroborated by the computer simulation.

When reconstructing actual data, the event distribution according to azimuthal reaction plane angle

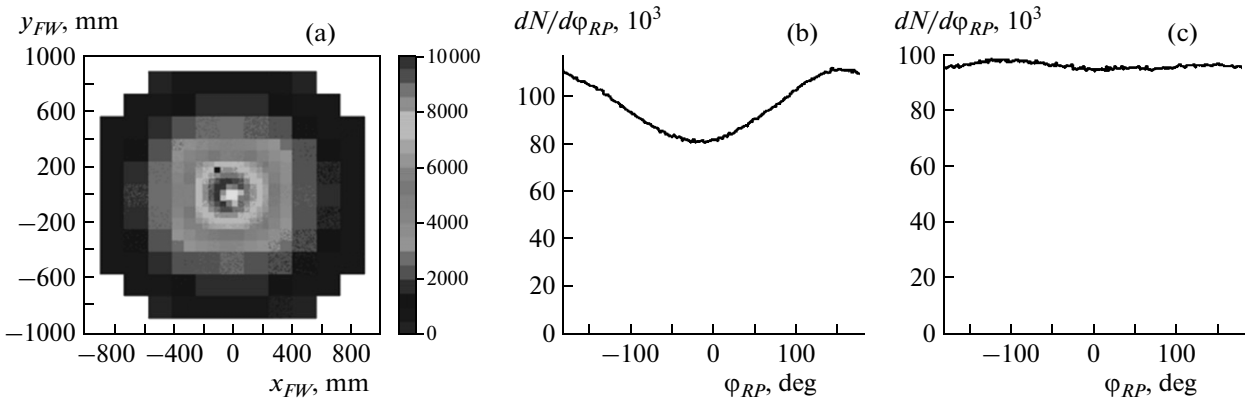

Fig. 21. (a) Experimental two-dimensional distribution determined by the occupancy of the hodoscope cells by spectators; (b) distribution in the reconstructed reaction plane angle corresponding to the experimental two-dimensional distribution; and (c) distribution in the reconstructed reaction plane angle after performing the procedure for centering at the beam position.

φ_{RP} obtained using Eq. (1) must be isotropic for events free from systematic distortions. However, in practice, obtained distribution $dN/d\varphi_{RP}$ often fails to be isotropic. This fact is illustrated by Fig. 21. Figure 21a shows the experimental two-dimensional distribution determined by the occupancy of the hodoscope cells by spectators before carrying out the procedure of centering at the beam position (with shades of gray corresponding to the counting rate), and Fig. 21b shows the event distribution in the reconstructed reaction plane angle.

The coordinates of hodoscope cell centers were used to reconstruct the orientation of the reaction plane, but the coordinate of the center of each triggered cell was uniformly smeared over the transverse dimensions of a cell. In Fig. 21a, one can see a small displacement of the beam axis with respect to the coordinates of the forward hodoscope center, which results in the systematic error in the values of the transverse momentum expressed in terms of the cell center coordinates (1).

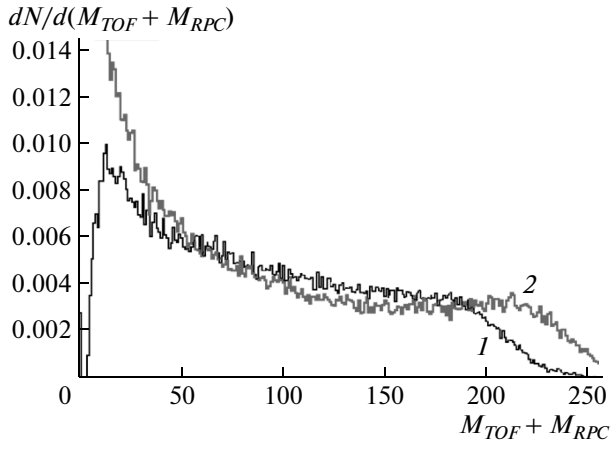

Fig. 22. Distributions in multiplicity M of secondary charged particles per one event, measured by the TOF and RPC detectors: (*1*) after the reconstruction of actual data and (*2*) obtained using total mathematical simulation.

Weight $\omega_k = 1$ was used as the first approximation in Eq. (1) when calculating the distribution in azimuthal reaction plane angle φ_{RP}. This approach appears to be better for attaining the angular anisotropy of the reconstructed reaction plane angle when the significant number of detector cells has problems with the dynamic range of the spectator charge measurements (in our case, ≈10% of the cells). In this case, the loss in the resolution of the reconstructed reaction plane angle is feeble. The obtained distribution of events in reconstructed reaction plane angle φ_{RP} is shown in Fig. 21b. One can easily discern a marked anisotropy caused by the small displacement of the beam center with respect to the coordinates of the forward hodoscope center.

Correction of the anisotropy in $dN/d\varphi_{RP}$ due to the displacement of the beam center with respect to the coordinates of the forward hodoscope center was performed using the correction of coordinates X_k and Y_k of the center of the forward hodoscope cells to the beam center position X_{bc}: $Y_k' = X_k - X_{\text{bc}}$ and $Y_k' = Y_k - Y_{\text{bc}}$. In the case of short-term variations of the beam center position due to the instability effects in the course of beam extraction, this correction can be made using event-by-event analysis.

After the coordinates of the forward hodoscope cell center are corrected with allowance for the mean beam position values and with neglect of the cells that are located in close vicinity to the forward hodoscope center and introduce an additional asymmetry upon displacement of the beam center, the event distribution in the reconstructed reaction plane angle obtained thereby takes the form shown in Fig. 21c. One can note its good agreement with the isotropic distribution.

The other abundant sources of systematic errors in the reconstructed reaction plane angle distribution may be the inefficiency of separate hodoscope cells

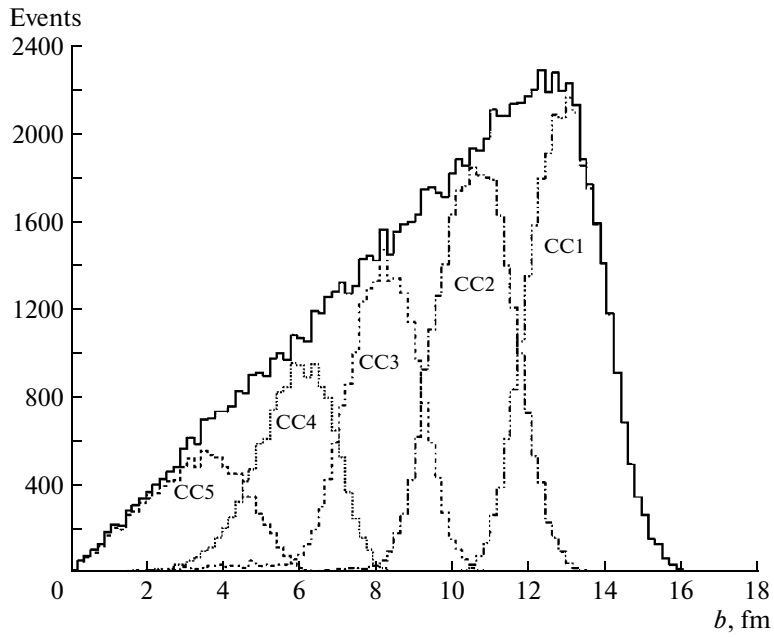

Fig. 23. Distributions in impact parameter b for the Au + Au reaction (1.24 GeV/nucleon) for five multiplicity ranges of secondary charged particles registered by the TOF and RPC detectors.

resulting in an azimuthal anisotropy, as well as certain azimuthal nonuniformity in the efficiency of the detectors participating in the trigger generation. The isotropy can be reconstructed using the so-called azimuthal leveling technique [18–20].

The Monte Carlo simulation of the collision reaction between 1.24-GeV/nucleon Au nuclei and Au nuclei in the immobile target system was performed to investigate the response of the forward hodoscope. The source event generator was the SHIELD program code [21] based on the multistage dynamic model including nuclear fragmentation [22]. The choice of this generator has been determined by the fact that collisions of nuclei generate fragments along with other secondary particles. Particles produced by this reaction were "guided" through the model of the HADES setup using the Geant program code, and the result obtained thereby was processed by the reconstruction program.

Figure 22 presents the distributions in the multiplicity of secondary charged particles per event, measured by the TOF and RPC detectors of the HADES after the reconstruction of real data (curve *1*) and after the reconstruction as part of the complete mathematical simulation (curve *2*). These data are largely in good agreement, except for the low-multiplicity region, where the distribution corresponding to the actual data is distorted by the multiplicity condition introduced by the trigger. Therefore, the use of the SHIELD generator in the simulation makes it possible to adequately reproduce distributions in the secondary charged particle multiplicity.

After analyzing the results of the described mathematical simulation procedure, five conventional classes corresponding to different centrality of events have been selected. These centrality classes (CCs) range from peripheral *CC1* to central *CC5* (Fig. 23). An interval of the total multiplicity of secondary charged particles registered by the TOF and RPC detectors corresponds to each CC. The described multiplicity intervals have been selected so that they do not overlap and can be used to select events by their centrality in actual data processing.

To estimate the resolution in azimuthal reaction plane angle φ_{RP} obtained with the forward hodoscope, we used the method of splitting an event into two identical subevents *A* and *B* in each of which the reaction plane angle was estimated [15]. The reaction plane angle was determined for events taken from different CCs. The selection by centrality was based on the charged particle multiplicity in the TOF and RPC detectors of the HADES. The distribution of the difference of the reaction plane angles for two subevents *A* and *B* is shown in Fig. 24 for five CCs, from *CC1* to *CC5*, where *CC1* corresponds to the peripheral events, *CC2* corresponds to the semi-peripheral events, and so on, and, finally, *CC5* corresponds to the central events. The σ values for the distributions in the difference of the reaction plane angles were 91.1°, 80.9°, 68.7°, 86.4°, and 92°, respectively.

The variance of the reaction plane distribution obtained from the triggered cells for the full event must be one-half the variance of the distribution in the difference of angles for two identical subevents [15]. The resolution obtained thereby is in good agreement with

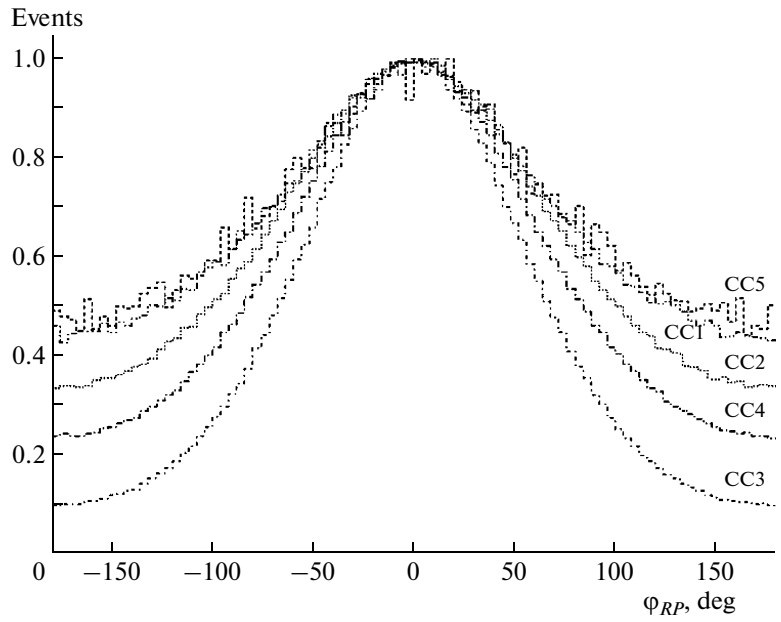

Fig. 24. Distributions of the difference of the reconstructed reaction plane angles from two identical subevents for five multiplicity ranges corresponding to different CCs.

the results of the KaoS experiment for the Au + Au reaction [19], which were obtained for a higher beam energy (1.5 GeV/nucleon). From the calculations, it is apparent that the best resolution is attained for semicentral events (for the impact parameter values close to 8 fm). For these events, the resolution estimated by the reconstructed reaction plane angle is ~34°. For the central and peripheral events, the resolution is estimated at ~46°.

ACKNOWLEDGMENTS

We thank the whole HADES collaboration team for the fruitful cooperation in developing the forward scintillation hodoscope and carrying out the tests and the physics experiments.

We also thank N.M. Sobolevskii for granting the SHIELD program generator.

REFERENCES

1. Cassing, W. and Bratkovskaya, E.L., *Phys. Rep.*, 1999, vol. 308, p. 65.
2. Porter, R.J., Beedoe, S., Bossingham, R., et al., *Phys. Rev. Lett.,* 1997, vol. 79, p. 1229.
3. Agakishiev, G., Balanda, A., Bannier, B., et al., *Eur. Phys. J., A: Hadrons and Nucl.,* 2009, vol. 41, p. 243.
4. Belver, D., Blanco, A., Cabanelas, P., Castro, E., Garzon, J.A., Zapata, M., Blanco, A., Carolino, N., Fonte, P., Lopes, L., Mangiarotti, A., Oliveira, O., Pereira, A., Silva, C., Diaz, J., Gil, A., Gonzalez-Diaz, D., Koenig, W., and Sousa, C.C., *Nucl. Instrum. Methods Phys. Res., A: Acceler., Spectrom., Detect. Assoc. Equipm.*, 2009, vol. 602, p. 687.
5. Agodi, C., Bassi, A., Bassini, R., Bellia, G., Coniglione, R., Cosentino, L., Finocchiaro, P., Maiolino, C., Piattelli, P., Sapienza, P., Spataro, S., Vassiliev, D., Iori, I., Boiano, C., Brambilla, S., Benovic, M., Hlavac, S., Turzo, I., Zovinec, D., Koenig, W., Kugler, A., Maiolino, C., Marek, T., Piattelli, P., Pleskač, R., Sapienza, P., Spataro, S., Suk, M., Taranenko, A., Tlustý, P., Turzo, I., Vassiliev, D., Wagner, V., and Zovinec, D., *Nucl. Instrum. Methods Phys. Res., A: Acceler., Spectrom., Detect. Assoc. Equipm.*, 2002, vol. 492, p. 14.
6. Lapidus, K., *Phys. Atom. Nucl.*, 2010, vol. 73, p. 985.
7. Senger, P., Ahner, W., Baltes, P., Beckerle, P., Bormann, C., Brill, D., Cies'lak, M., Grosse, E., Henning, W., Koczon', P., Kohlmeyer, B., Konrad, W., Miskowiec, D., Müntz, C., Oeschler, H., Pöppl, H., Prokopowicz, W., Pühlhofer, F., Sartorius, S., Schicker, R., Schlei, B., Schwab, E., Shin, Y., Speer, I., Stein, J., Stiebing, K., Stock, R., Ströbele, H., Sturm, C., Völkel, K., Wagner, A., and Walus', W., *Nucl. Instrum. Methods Phys. Res., A: Acceler., Spectrom., Detect. Assoc. Equipm.*, 1993, vol. 327, p. 393.
8. Frohlich, I., Kajetanowicz, M., Korcyl, K., Krzemien, W., Palka, M., Salabura, P., Schrader, C., Skott, P., Strobele, H., Stroth, J., Tarantola, A., Traxler, M., Trebacz, R., and Yurevich, S., *IEEE Trans. Sci.*, 2008, vol. 55, p. 59.
9. Mota, M. and Christiansen, J., *IEEE J. Solid-State Circuits*, 1999, vol. 34, p. 123.
10. Anghinolfi, F., Jarron, P. Martemiyanov, A.N., Usenko, E., Wenninger, H., Williams, M.C.S., and Zichichi, A., *Nucl. Instrum. Methods Phys. Res., A: Acceler., Spectrom., Detect. Assoc. Equipm.*, 2004, vol. 533, p. 183.
11. Agakishiev, G., Agodi, C., Badala, A., et al., *Eur. Phys. J., A: Hadrons and Nuclei*, 2009, vol. 40, p. 45.

12. Agakishiev, G., Badala, A., Belver, D., et al., *Phys. Lett. A.*, 2010, vol. 690, p. 118.
13. Lapidus, K., *Candidate Sci. (Phys.-Math.) Dissertation*, Inst. Nucl. Res. Russ. Acad. Sci. http://www.dissercat.com/content/obrazovanie-elektron-pozitronnykh-par-v-kvazisvobodnykh-neitron-protonnykh-stolknoveniyakh
14. Gyulassy, M., *Phys. Lett. A.*, 1982, vol. 110, p. 185.
15. Danielewicz, P. and Odyniec, G., *Phys. Lett. A.*, 1985, vol. 157, p. 168.
16. Fai, G. and Randrup, J., *Comp. Phys. Commun.,* 1986, vol. 42, p. 385.
17. Taranenko, *A., Ph. D. Thesis*, Prague: Charles University, 2001.
18. Uhlig, F., *Ph. D. Thesis*, Darmstadt: Tech. Univ., 2003.
19. Foerster, A., *Ph. D. Thesis*, Darmstadt: Tech. Univ., 2003.
20. Ploskon, M., *Ph. D., Thesis,* Univ. Frankfurt, 2005.
21. http://www.inr.ru/shield/
22. Botvina A.S., Dementyev A.V., Smirnova O.N. et al., *MSDM—Multy Stage Dynamical Model. In International Codes and Model Inter comparison for Intermediate Energy Activation Yields*, Michel, R. and Nagel, P., Eds., NSC/DOC(97)-1, NEA/P&T, no. 14. OECD, Paris, 1997, p. 307.

Translated by N. Goryacheva